



MOSEL: Strong [O III] 5007 Å Emitting Galaxies at ($3 < z < 4$) from the ZFOURGE Survey

Kim-Vy H. Tran^{1,2,3}, Ben Forrest⁴, Leo Y. Alcorn^{2,13}, Tiantian Yuan^{3,5}, Themiya Nanayakkara⁶, Jonathan Cohn², Michael Cowley^{7,8}, Karl Glazebrook^{3,5}, Anshu Gupta^{1,3}, Glenn G. Kacprzak^{3,5}, Lisa Kewley^{3,9}, Ivo Labbé⁵, Casey Papovich², Lee Spitler^{3,10}, Caroline M. S. Straatman¹¹, and Adam Tomczak¹²

¹School of Physics, University of New South Wales, Kensington, Australia; kimvy.tran@gmail.com

²George P. and Cynthia W. Mitchell Institute for Fundamental Physics and Astronomy, Department of Physics & Astronomy, Texas A&M University, College Station, TX 77843, USA

³ARC Centre for Excellence in All-Sky Astrophysics in 3D (ASTRO 3D), Australia

⁴Department of Physics & Astronomy, University of California, Riverside, CA 92521, USA

⁵Swinburne University of Technology, Hawthorn, VIC 3122, Australia

⁶Leiden Observatory, Leiden University, P.O. Box 9513, NL 2300 RA Leiden, The Netherlands

⁷Centre for Astrophysics, University of Southern Queensland, West Street, Toowoomba, QLD 4350, Australia

⁸School of Chemistry, Physics and Mechanical Engineering, Queensland University of Technology, Brisbane, QLD 4001, Australia

⁹Research School of Astronomy and Astrophysics, The Australian National University, Cotter Road, Weston Creek, ACT 2611, Australia

¹⁰Department of Physics and Astronomy, Faculty of Science and Engineering, Macquarie University, Sydney, NSW 2109, Australia

¹¹Sterrenkundig Observatorium, Universiteit Gent, Krijgslaan 281 S9, B-9000 Gent, Belgium

¹²Department of Physics, University of California, Davis, One Shields Avenue, Davis, CA 95616, USA

Received 2019 July 4; revised 2020 April 17; accepted 2020 April 22; published 2020 July 21

Abstract

To understand how strong emission-line galaxies (SELGs) contribute to the overall growth of galaxies and star formation history of the universe, we target SELGs from the ZFOURGE imaging survey that have blended H β + [O III] rest-frame equivalent widths of >230 Å and $2.5 < z_{\text{phot}} < 4.0$. Using Keck/MOSFIRE, we measure 49 redshifts for galaxies brighter than $K_s = 25$ mag as part of our Multi-Object Spectroscopic Emission Line (MOSEL) survey. Our spectroscopic success rate is $\sim 53\%$ and z_{phot} uncertainty is $\sigma_z = [\Delta z / (1+z)] = 0.0135$. We confirm 31 ELGs at $3 < z_{\text{spec}} < 3.8$, and show that SELGs have spectroscopic rest-frame [O III]5007 Å equivalent widths of 100–500 Å and tend to be lower-mass systems [$\log(M_*/M_\odot) \sim 8.2$ – 9.6] compared with more typical star-forming galaxies. The SELGs lie ~ 0.9 dex above the star-forming main sequence at $z \sim 3.5$ and have high inferred gas fractions of $f_{\text{gas}} \gtrsim 60\%$, i.e., the inferred gas masses can easily fuel a starburst to double stellar masses within ~ 10 – 100 Myr. Combined with recent results using ZFOURGE, our analysis indicates that (1) strong [O III] 5007 Å emission signals an early episode of intense stellar growth in low-mass [$M_* < 0.1 M^*$] galaxies and (2) many, if not most, galaxies at $z > 3$ go through this starburst phase. If true, low-mass galaxies with strong [O III] 5007 Å emission ($\text{EW}_{\text{rest}} > 200$ Å) may be an increasingly important source of ionizing UV radiation at $z > 3$.

Unified Astronomy Thesaurus concepts: Emission line galaxies (459); Galaxy evolution (594); Galaxy formation (595); Starburst galaxies (1570); Galaxy properties (615); Near infrared astronomy (1093)

1. Introduction

Hierarchical formation predicts that massive galaxies, like the Milky Way, grow through the merger and accretion of smaller systems (Peebles 1970), thus low-mass, chemically pristine galaxies can provide insight into the early stages of galaxy formation. Although low-mass galaxies are abundant, identifying those that are the least chemically evolved via emission lines is difficult, due to their rare nature in the local universe. In the past decade, dwarf galaxies with strong [O III]5007 Å emission at $z \lesssim 0.3$ (Cardamone et al. 2009; Izotov et al. 2011) have been identified using optical imaging where the large equivalent width of the emission line increases the broadband flux. Valuable insight is gained by measuring, e.g., star formation conditions and ionizing escape fractions (Amorín et al. 2012; Jaskot & Oey 2013; Bian et al. 2016; Izotov et al. 2016, 2018; Lofthouse et al. 2017), in these local “green pea” galaxies. For example, studies find that strong H β + [O III]5007 Å emission are ubiquitous in Lyman-break galaxies at $z \sim 7$ (Smit et al. 2014).

A number of studies have now identified dwarf galaxies ($\log(M_*/M_\odot) \lesssim 9$) at $0 < z < 2$ with strong [O III]5007 Å emission that may bridge local “green peas” to primeval galaxies

at $z > 6$. Slit-less, near-infrared spectroscopy with the Hubble Space Telescope revealed a population of dwarf galaxies up to $z \sim 2$ with rest-frame [O III]5007 Å equivalent widths of $\text{EW}_{\text{rest}} > 200$ Å (e.g., Straughn et al. 2009; Atek et al. 2011; van der Wel et al. 2011). Dedicated ground-based spectroscopic surveys also identified strong emission-line galaxies (SELGs) up to $z \sim 1$ (Amorín et al. 2015). These studies suggest that the number density of SELGs increases with redshift (e.g., Masada et al. 2018). However, quantifying the evolving number density of strong [O III]5007 Å emitting galaxies at $z > 1$ requires near-infrared spectroscopy ($\lambda > 1 \mu\text{m}$), thus only a handful of systems have been confirmed at $z \gtrsim 3$ (de Barros et al. 2016; Nakajima et al. 2016; Amorín et al. 2017).

Once identified, the natural question then is how these strong [O III]5007 Å emitting galaxies fit into our existing picture of galaxy formation. The increasing number of SELGs, combined with the brief duration of this intense starburst phase ($\lesssim 100$ Myr; Guo et al. 2016; Ceverino et al. 2019), supports a model in which galaxies grow through multiple intense starbursts. For starburst systems at $z \gtrsim 3$ with low metallicities, such an episode can signal the initial major growth spurt, i.e., the emission-line galaxies (ELGs) with the highest equivalent widths ($\text{EW}_{\text{rest}} \gtrsim 1000$ Å) are “first burst” systems (Cohn et al. 2018). In combination with

¹³ LSSTC Data Science Fellow.

studies of, e.g., Lyman-break galaxies at $z \sim 7$ with strong $H\beta + [\text{O III}]5007 \text{ \AA}$ emission (Roberts-Borsani et al. 2016), we can use SELGs to test current galaxy formation models that capture the intricate interplay of physics on the subkpc scale with the integrated galaxy properties that can be measured at $z > 2$ (Krumholz et al. 2017).

An increasing population of SELGs with redshift also has important implications for cosmic reionization. These vigorously star-forming galaxies have steep UV slopes ($\beta \lesssim -2$) and low metallicities ($Z/Z_{\odot} \lesssim 0.2$; Cohn et al. 2018; Forrest et al. 2018), i.e., the SELGs may be a tremendous source of UV photons. By identifying the strong $[\text{O III}]5007 \text{ \AA}$ emitting galaxies, we can then measure their Lyman-continuum emission and escape fractions to infer if SELGs at $z > 8$ can generate the UV photons needed to reionize the universe (Ouchi et al. 2009; Mitra et al. 2013; Robertson et al. 2015). Ideally, we would track SELGs from $z \sim 0$ to the first galaxies at $z > 8$. However, current near-infrared instruments place a redshift limit of $z \sim 4$ for identifying the $[\text{O III}]5007 \text{ \AA}$ emitters that are the focus of our study.

An effective method to identify galaxies with strong $[\text{O III}]5007 \text{ \AA}$ emission ($\text{EW}_{\text{rest}} > 200 \text{ \AA}$) at $z \gtrsim 2$ is to first use deep multiband photometry to select candidates and then confirm with near-IR spectroscopy. The ELGs with the strongest $[\text{O III}]5007 \text{ \AA}$ emission tend to be low-mass ($\log(M_{*}/M_{\odot}) < 9.5$; e.g., Maseda et al. 2013, 2014) systems, thus sensitive multiwavelength imaging is needed to push down in the stellar mass to select candidates. Precise photometric redshifts at $z > 1$ also are essential for identifying strong emission-line features in the spectral energy distributions (SEDs), and this requires medium-band, near-IR imaging. Last, only with deep near-IR spectroscopy can the extreme $[\text{O III}]5007 \text{ \AA}$ nature of these systems be confirmed.

With the advent of deep near-IR imaging surveys and sensitive near-IR spectrographs, we are now able to identify these strong $[\text{O III}]5007 \text{ \AA}$ emitting galaxies at $z \sim 3-4$. Our method is similar to studies that couple near-IR imaging and near-IR spectroscopy to identify galaxies with strong equivalent widths at $z \sim 1-2$, e.g., 3D-HST (Maseda et al. 2013, 2014, 2018). First, we use the ZFOURGE survey that measures precise photometric redshifts to $\sim 70,000$ objects by combining deep imaging with medium-band, near-IR filters $J_1 J_2 J_3 H_s H_i K_s$ and public multiwavelength observations (redshift uncertainties of $\sigma_z \sim 1.6\%$; Straatman et al. 2016). At $z \sim 3$, the ZFOURGE survey is 80% mass-complete to $\log(M_{*}/M_{\odot}) \sim 9.5$ and measures star formation rates down to $\sim 5 M_{\odot} \text{ yr}^{-1}$ (Tomczak et al. 2016).

With photometry spanning observed UV to mid/far-IR, we then construct composite SEDs that are defined by the underlying galaxy populations (Kriek et al. 2011; Forrest et al. 2016). In our analysis of ZFOURGE galaxies at $2.5 < z_{\text{phot}} < 4.0$, we discovered a population of ~ 80 galaxies with blended rest-frame $H\beta + [\text{O III}]$ equivalent widths in excess of $\sim 800 \text{ \AA}$ (Forrest et al. 2017). In comparison, there are only ~ 14 galaxies with such extreme $H\beta + [\text{O III}]$ at $1 < z < 3$ (Forrest et al. 2018). The rapid increase in the number density of the extreme $H\beta + [\text{O III}]$ emitting galaxies from $z \sim 2$ to $z \sim 3.5$ suggests potentially explosive growth at higher redshift (see also van der Wel et al. 2011).

To spectroscopically confirm the $H\beta + [\text{O III}]$ emitting galaxies identified in ZFOURGE, we introduce our Multi-Object Spectroscopic Emission Line (MOSEL¹⁴) survey. In this

paper, we focus on ELGs at $2.5 < z_{\text{phot}} < 4.0$ to measure their redshifts and rest-frame $[\text{O III}]5007 \text{ \AA}$ equivalent widths and line widths. We combine our spectroscopic measurements with physical properties obtained from deep multiband imaging to infer gas fractions and virial masses, and test disk formation models.

By identifying SELGs up to $z \sim 4$ (Forrest et al. 2017, 2018), MOSEL complements existing emission-line searches conducted with the Hubble Space Telescope. Due to the wavelength ranges of the WFC3 and ACS grisms, blind spectroscopic surveys such as 3D-HST (Momcheva et al. 2016), WISP (Atek et al. 2011), and PEARS (Straughn et al. 2008) are limited to SELGs at $z \lesssim 2.3$. Our medium-band NIR imaging from ZFOURGE combined with public legacy data sets enables us to reach comparable stellar masses as the blind spectroscopic surveys ($\log(M_{*}/M_{\odot}) \sim 8.5$ at $z \sim 1$; Straatman et al. 2016). At $z \sim 3-4$, we also span comparable ranges in rest-frame equivalent width ($\gtrsim 200 \text{ \AA}$) and spectral line flux ($\sim 1-2 \times 10^{-17} \text{ erg s}^{-1} \text{ cm}^{-2} \text{ \AA}^{-1}$) as the lower redshift studies.

In our analysis, we use AB magnitudes and the galaxy parameters measured by Forrest et al. (2017, 2018) for the ZFOURGE data set. FAST (Kriek et al. 2009) is used to fit the SEDs assuming a Chabrier Initial Mass Function and an SED library with one-fifth solar metallicity and emission lines (see Salmon et al. 2015; Forrest et al. 2018). We assume $\Omega_m = 0.3$, $\Omega_{\Lambda} = 0.7$, $H_0 = 70 \text{ km s}^{-1} \text{ Mpc}^{-1}$, and a flat universe; the corresponding angular scale at $z = 3.0$ is 7.7 kpc per arcsec.

2. Data and Methods

2.1. Selecting Emission-line Galaxies

The following summarizes the ZFOURGE observations used to measure photometric redshifts and galaxy properties and to generate the composite SEDs. For complete descriptions of the data products used here, we refer the reader to the ZFOURGE survey paper by Straatman et al. (2016) and the analysis of star formation rates by Tomczak et al. (2016).

2.1.1. ZFOURGE Imaging Catalogs

We use the deep near-IR imaging from the FourStar Galaxy Evolution survey (ZFOURGE; Straatman et al. 2016) obtained with the FourStar imager (Persson et al. 2013) on the Magellan Telescope of three legacy fields: CDFS (Giacconi et al. 2002), COSMOS (Scoville et al. 2007), and UDS (Lawrence et al. 2007). ZFOURGE divides the J -band filter into J_1 , J_2 , and J_3 and the H -band filter into H_s and H_i ; ZFOURGE also obtains deep K_s imaging that is used as the detection image. In combination with existing multiwavelength observations, ZFOURGE provides high precision photometric redshifts with $\sigma_z = 0.016$ (Straatman et al. 2016) for over 70,000 objects; the redshift precision is confirmed by the ZFIRE spectroscopic survey (Nanayakkara et al. 2016).

We incorporate HST imaging from CANDELS (Grogin et al. 2011; Koekemoer et al. 2011) spanning $0.3-1.6 \mu\text{m}$ to measure photometry and galaxy properties. We also use Spitzer/IRAC (all four channels) and MIPS data ($24 \mu\text{m}$) for the CDFS, COSMOS, and UDS fields (GOODS-S: PI Dickinson, COSMOS: PI Scoville, UDS: PI Dunlop), and 100 and $160 \mu\text{m}$ for CDFS. For CDFS only, we include public Herschel/PACS data (Elbaz et al. 2011). Total star formation rates are calculated by combining the UV and IR contributions; see Tomczak et al. (2016, Section 2) for a detailed description.

¹⁴ Mosel is also one of the 13 official German wine regions (Weinbauggebiete), known for Riesling and Pinot Noir.

2.1.2. Candidate Emission-line Galaxies at $2.5 < z_{\text{phot}} < 4.0$

ZFOURGE is particularly sensitive to emission-line galaxies at $2.5 < z_{\text{phot}} < 4.0$ because $\text{H}\beta + [\text{O III}]$ emission falls in the deep K_s imaging. To identify galaxies with the strongest emission lines, we use the composite SEDs generated by Forrest et al. (2017). From testing multiple fitting methods, Forrest et al. (2018, Section 4.5) show that rest-frame equivalent widths down to $\sim 20 \text{ \AA}$ can be recovered from the composite SEDs; in the case of $\text{H}\beta + [\text{O III}]$, the detection threshold applies to the blended EW_{rest} .

To summarize, we iteratively select the *primary galaxies* with the largest number of *analog galaxies* based on the similarity of 22 rest-frame UVOIR colors ($b < 0.05$, from Kriek et al. 2011; Forrest et al. 2016) to collectively form separate *composite groups*. Observed photometry from analog galaxies in each composite group are then deredshifted, normalized to a common flux scale, and combined to build a composite SED, essentially a low-resolution ($R \sim 40$) spectrum.

We focus on the two composite SEDs from Forrest et al. (2017, 2018) with the steepest UV slope and strongest blended $\text{H}\beta + [\text{O III}]$ emission. We adopt an admittedly arbitrary definition and refer to these emission-line galaxies as *strong* (SELG). In our analysis, we refer to the following types of galaxies:

1. Star-forming galaxy (SFG): composite SEDs with rest-frame $\text{H}\beta + [\text{O III}]$ equivalent widths of $< 230 \text{ \AA}$.
2. SELG: the combined sample of 278 galaxies in S_1ELG and S_2ELG .
3. S_1ELG : the 60 galaxies grouped in the the composite SED with rest-frame $\text{H}\beta + [\text{O III}]$ equivalent width of $> 800 \text{ \AA}$.
4. S_2ELG : the 218 galaxies grouped in the the composite SED with rest-frame $\text{H}\beta + [\text{O III}]$ equivalent width of $230\text{--}800 \text{ \AA}$.

Across the three ZFOURGE fields, we identify a total of 278 candidate SELGs from the ZFOURGE composite SEDs, the majority of which are in CDFS (Forrest et al. 2017). Except where noted, we use the combined sample of SELGs = ($\text{S}_1\text{ELG} + \text{S}_2\text{ELG}$). We exclude active galactic nuclei (AGNs) identified by Cowley et al. (2016) by using multiwavelength diagnostics; we discuss this in more detail in Section 3.7.

2.2. Keck/MOSFIRE Spectroscopy

2.2.1. Observations

We used MOSFIRE (McLean et al. 2012) on Keck I (project code Z245, PI: Kewley) on 2017 February 12 and 13. We observed five masks in COSMOS and one mask in CDFS. To measure $\text{H}\beta + [\text{O III}]$ at $z \sim 3$, we used the K band with a wavelength range of $1.93\text{--}2.38 \mu\text{m}$ and a spectral dispersion of $2.17 \text{ \AA pixel}^{-1}$. We used an AB dither pattern with $1''.5$ nod and integrated each mask for a total on-sky time of 96 minutes (110 minutes clock time); seeing ranged from $0''.7\text{--}1''$.

In the six MOSFIRE masks, we targeted a total of 105 galaxies at $0.9 < z_{\text{phot}} < 4.8$, where the highest-priority targets were the 38 SELGs candidates at $2.5 < z_{\text{phot}} < 4.0$. The remaining targets (67) primarily were star-forming galaxies at $2 < z_{\text{phot}} < 4$. Each mask included a flux monitor star to anchor the spectrophotometric calibrations. We follow the same reduction pipeline as in our ZFIRE survey (Tran et al. 2015, 2017; Nanayakkara et al. 2016), and estimate a 3σ line-flux limit in the MOSFIRE K band of $\sim 3 \times 10^{-18} \text{ erg s}^{-1} \text{ cm}^{-2}$.

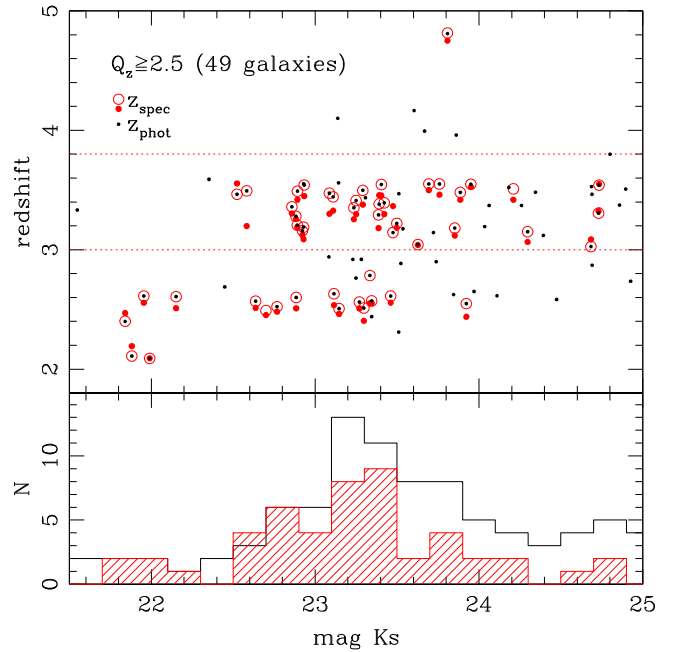


Figure 1. We compare the photometric redshifts (top) and K_s magnitudes (bottom) of the 95 targeted galaxies (small filled black circles and open black histograms) with the 49 galaxies with spectroscopic redshifts (vertical pairs of large filled and open red circles and hashed red histograms). The median z_{spec} of these 49 galaxies is only $\sim 1\%$ lower than their median z_{phot} (3.19 vs. 3.22). Our analysis focuses on the 31 spectroscopically confirmed galaxies at $3 < z_{\text{spec}} < 3.8$, where $\text{H}\beta + [\text{O III}]$ fall in the MOSFIRE K band (top panel, horizontal dashed lines).

Note that the angular sizes of the galaxies are comparable with or smaller than the slit width of $0''.7$ (Figure 7); i.e., there should be no significant systematic error such as slit-loss due to the spectrophotometric calibration.

2.2.2. Spectroscopic Redshifts

Of the 105 galaxies targeted with MOSFIRE, we measure spectroscopic redshifts for 49 ($2.091 < z_{\text{spec}} < 4.751$; see Figure 1). Considering only the 89 targeted galaxies with photometric redshifts in the same range, i.e., galaxies where $[\text{O III}]$ and $\text{H}\alpha$ fall in the K band, our success rate is $\sim 53\%$. The 49 galaxies with spectroscopic redshifts have K_s magnitudes brighter than 25 and quality flag of $Q_z \geq 2.5$. In our analysis, $Q_z \geq 2.5$ means that the spectral line emission matches the ZFOURGE photometric redshift, or there are two spectral lines with the same redshift (for all definitions of Q_z , see Nanayakkara et al. 2016).

On average, z_{phot} is ~ 0.054 higher than z_{spec} (Figure 1) and the corresponding uncertainty is $\sigma_z = [\Delta z / (1+z)] = 0.0135$. The largest outliers have $\Delta z \sim 0.3$ and $\sigma_z \sim 0.07$. A two-sample Kolmogorov–Smirnov (K-S) test shows the probability that the spectroscopically confirmed sample and the targeted sample are drawn from the same parent z_{phot} distribution to be 3.6%; i.e., the two distributions are different at the 2σ level. The spectroscopically confirmed sample also is ~ 0.25 magnitudes brighter with a K-S probability of being drawn from the same parent K_s distribution as the targeted sample of 15%.

Of the 13 targeted S_1ELG that were grouped in the composite SED with the highest $\text{H}\beta + [\text{O III}]$ emission ($\text{EW}_{\text{rest}} > 800 \text{ \AA}$), two were lost due to mechanical problems with configuring the mask and two had no measured redshift. The median redshift of the nine confirmed ELGs is

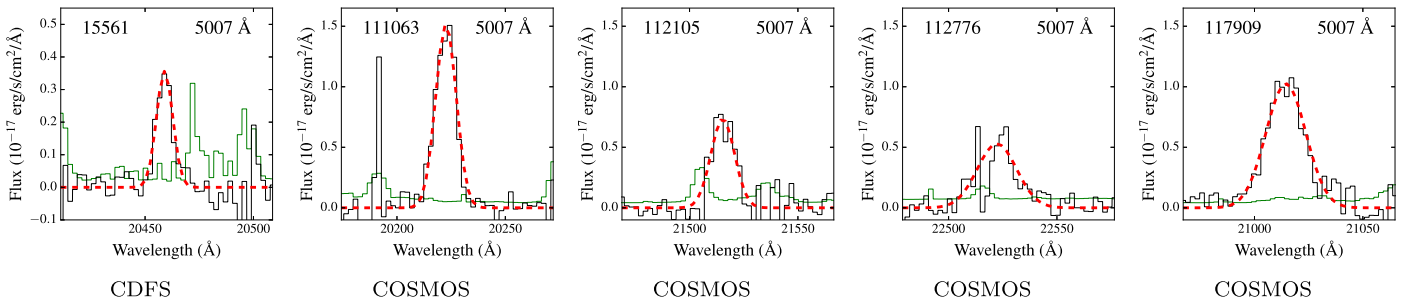


Figure 2. Example of fits to the MOSFIRE spectra (Section 2.2.3) showing the observed 1D spectrum (black), the 1D error spectrum (green), and the 1D Gaussian fit (red dashed curve).

$z_{\text{spec}} = 3.189$ compared with their median $z_{\text{phot}} = 3.207$. The corresponding uncertainty of $\sigma_z = 0.42\%$ is even lower than that of our ZFIRE survey, which targeted a broader selection of galaxies at $z \sim 2$ (Tran et al. 2015; Nanayakkara et al. 2016). Note also that the largest outliers are $\Delta z \sim 0.1$, which is a factor of three smaller compared with the SFGs ($\Delta z \sim 0.3$). In our analysis, we focus on the eight ELGs at $3 < z_{\text{spec}} < 3.8$ and exclude the ELG at $z_{\text{spec}} = 2.549$ (ID 4791).

Of the 25 targeted S₂ELG that were grouped in the composite SED with the second-highest H β + [O III] emission ($230 < EW_{\text{rest}} < 800 \text{ \AA}$), 13 were spectroscopically confirmed with a median redshift of $z_{\text{spec}} = 3.327$ compared with their median $z_{\text{phot}} = 3.41$. The corresponding uncertainty of $\sigma_z = 1.9\%$ for the S₂ELG is larger than that of the S₁ELG and more typical of the ZFOURGE survey as a whole (Nanayakkara et al. 2016; Straatman et al. 2016). All 13 have redshifts of $3 < z_{\text{spec}} < 3.8$.

Of the remaining 67 galaxies targeted with MOSFIRE, 28 have spectroscopic redshifts (Figure 1) with a median redshift of $z_{\text{spec}} = 2.551$ compared with their median $z_{\text{phot}} = 2.612$. In our analysis, we focus on the 10 SFGs at $3 < z_{\text{spec}} < 3.8$; i.e., we exclude the 17 galaxies at $z_{\text{spec}} < 2.6$ and the one galaxy at $z_{\text{spec}} = 4.815$. We note that due to decreasing throughput of the near-IR arrays at $\lambda \gtrsim 2.2 \mu\text{m}$, the redshift cutoff is effectively $z \sim 3.6$, except for objects with the strongest [O III]5007 Å emission.

2.2.3. Measuring [O III]5007 Å Spectral Line Emission

Following Alcorn et al. (2016, 2018), we first extract a 1D spectrum from an aperture defined by the 1σ Gaussian width of the [O III]5007 Å emission line along the spatial direction (Figure 2). To determine the [O III]5007 Å line flux, we integrate the best-fit Gaussian centered on the line emission along the wavelength direction using the 3σ range; all line fits are visually inspected for quality control. We subtract in quadrature the instrumental broadening from the measured line width and then convert to an integrated velocity dispersion (σ_{int}) using the galaxy’s measured redshift. Errors in σ_{int} are estimated by adding sky noise to the observed spectrum and refitting 1000 times.

2.2.4. Determining [O III]5007 Å Equivalent Width

To measure [O III]5007 Å equivalent widths requires both line and continuum flux. However, most of the ELGs are too faint to directly measure their continua from the MOSFIRE spectroscopy. We use the method described in Nanayakkara et al. (2017) that combines our spectrophotometrically calibrated [O III]5007 Å line fluxes with the deep continuum photometry from ZFOURGE (Straatman et al. 2016). Because

the ZFOURGE photometry provides a better measurement of the faint continuum relative to the spectroscopy, the primary source of uncertainty is thus due to systematic error of the spectrophotometric calibration, and this uncertainty is of order $\sim 10\%$ – 20% for continuum-detected galaxies (Nanayakkara et al. 2016). Note that given the galaxy sizes are comparable with or smaller than the slit width of (Figure 7), the systematic error due to the spectrophotometric calibration is not significant.

To determine the continuum for each ELG, we use the FAST fits (Kriek et al. 2009) from Forrest et al. (2017, 2018) that include a template library with strong emission lines. As we show in both Cohn et al. (2018) and Forrest et al. (2018), the stellar masses for low-mass galaxies ($\log(M_*/M_\odot) \lesssim 10$) can be overestimated by ~ 0.5 – 0.7 dex if strong emission lines are not included in the SED modeling. The emission lines are from Salmon et al. (2015), who couple the photoionization code Cloudy (Ferland et al. 2013) with BC03 simple stellar populations (Bruzual & Charlot 2003) as the ionizing source to generate nebular emission models.

Because both star formation rate and stellar mass depend on the adopted stellar metallicity, SED fits are generated for solar ($Z = 0.02$) and subsolar ($Z = 0.004$) values. The strong emission lines indicate the ELGs have gas metallicities lower than solar, thus we use the subsolar stellar metallicity fits ($Z = 0.004$; see also Cohn et al. 2018). However, we stress that the value adopted for the metallicity does not change the measured value for the continuum nor the measured EW_{rest} , only how we interpret the measurements.

We calculate the observed frame continuum on the blue and red side of the H β + [O III] lines by using top-hat filters (width of 150 Å) centered at 4675 Å and 5200 Å on the best-fit FAST SED. We then divide the observed [O III]5007 Å line flux by the average observed continuum and the galaxy redshift:

$$EW_{\text{rest}}(5007) = \frac{f_{\text{line}}(5007)}{[(f_{\text{cont}}(4675) + f_{\text{cont}}(5200))/2] \left(\frac{1}{1+z} \right)}. \quad (1)$$

For a line flux of $3 \times 10^{-18} \text{ erg s}^{-1} \text{ cm}^{-2}$ and continuum flux of $5 \times 10^{-20} \text{ erg s}^{-1} \text{ cm}^{-2} \text{ \AA}^{-1}$ (approximately K_s magnitude of 24.0), the observed equivalent width is 60 Å; for a galaxy at $z_{\text{spec}} = 3.0$, the corresponding rest-frame equivalent width is $EW_{\text{rest}} = 15 \text{ \AA}$. For comparison, the lowest values we measure for the spectral rest-frame equivalent widths using MOSFIRE are $\sim 20 \text{ \AA}$ (Table 2). We note that Forrest et al. (2018, Section 4.5) estimated rest-frame EW_{rest} down to $\sim 20 \text{ \AA}$ can be measured from the composite SEDs.

For reference, the 3D-HST survey quotes a 3σ emission-line-flux limit for point sources of $1.5 \times 10^{-17} \text{ erg s}^{-1} \text{ cm}^{-2}$ (Momcheva et al. 2016). Assuming the same continuum flux

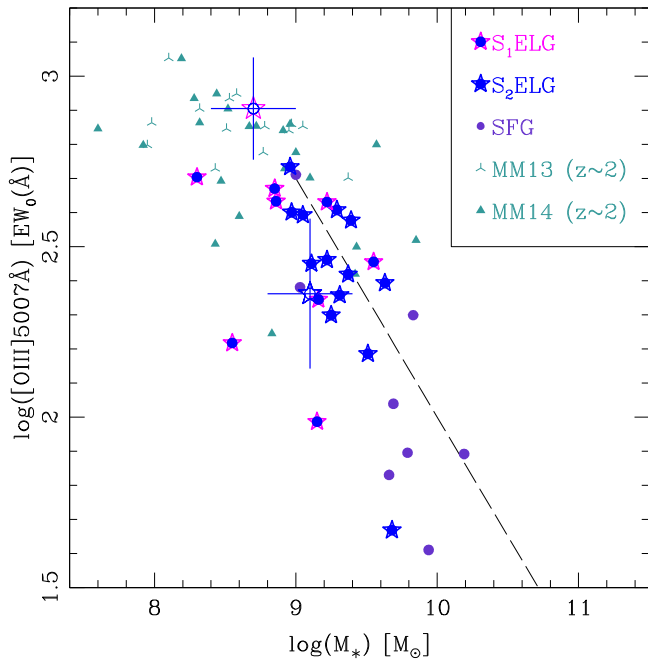


Figure 3. Spectroscopic rest-frame [O III]5007 Å equivalent widths for confirmed ELGs at $3 < z_{\text{spec}} < 3.8$; typical uncertainties in the stellar mass are ~ 2 (Forrest et al. 2018). The symbols denote galaxy classifications as defined by the Composite SEDs, i.e., from photometry only, and the large open stars show the rest-frame blended $H\beta + [\text{O III}]$ equivalent width as measured from the two composite SEDs with the strongest emission from Forrest et al. (2017). Shown are (1) S_1 ELG with blended rest-frame $H\beta + [\text{O III}]$ $EW_{\text{rest}} > 800$ Å as measured from their Composite SED; (2) S_2 ELG with blended rest-frame $H\beta + [\text{O III}]$ $EW_{\text{rest}} \sim 230$ – 800 Å; and (3) more typical star-forming galaxies with blended rest-frame $H\beta + [\text{O III}]$ $EW_{\text{rest}} < 230$ Å. For comparison, SELGs at $1 < z < 3$ selected with 3D-HST (Maseda et al. 2013, 2014) are shown in cyan; the spectral resolution and flux limit of the grism observations selects ELGs with the highest [O III]5007 Å EWs. The dashed line shows the average relationship between [O III]5007 Å EW_{obs} and stellar mass from MOSDEF for galaxies at $z \sim 2$ (Reddy et al. 2018).

level, their limit corresponds to an observed equivalent width of 300 Å, i.e., approximately five times higher than MOSEL.

3. Results

In our analysis, we focus on the 31 galaxies that are spectroscopically confirmed to be at $3 < z_{\text{spec}} < 3.8$ (Figure 1). We measure the [O III]5007 Å emission for these galaxies with our K -band spectroscopy (Figure 2). We combine our spectral measurements with deep photometry from ZFOURGE to measure continuum properties, and use galaxy sizes from van der Wel et al. (2012). Although the $L_{\text{UV+IR}}$ -based SF rates from Tomczak et al. (2016) based on solar metallicity models are robust to significant flux from line emission, the stellar masses can be overestimated by as much as a factor of ~ 2 (e.g., Cohn et al. 2018; Forrest et al. 2018). For these galaxies, we use stellar masses determined through the use of updated FAST fits that include an SED template with strong emission lines and one-fifth solar metallicity ($Z = 0.004$; Forrest et al. 2018).

3.1. Strong [O III]5007 Å Emission

With our MOSFIRE spectroscopy and deep multiband imaging, we estimate rest-frame [O III]5007 Å equivalent widths using the hybrid method described in Section 2.2.4. Our spectroscopically confirmed SELGs span similar ranges with [O III]5007 Å $EW_{\text{rest}} \sim 100$ – 500 Å (Figure 3). These

ranges are consistent with the large blended $H\beta + [\text{O III}]$ equivalent widths ($EW_{\text{rest}} \gtrsim 200$ Å) measured from their composite SEDs (Forrest et al. 2017, 2018).

The SELGs at $3 < z_{\text{spec}} < 3.8$ show a trend of decreasing [O III]5007 Å equivalent width with increasing stellar mass that is also observed in SELGs at $z \sim 2$ (Figure 3; Maseda et al. 2014). The significant overlap between S_1 ELG and S_2 ELG indicates that the two are not distinctly different populations. Note that the SELGs at $z \sim 2$ include systems with $\log(M_*/M_\odot) \sim 8$ while our $z \sim 3$ – 4 SELGs have $\log(M_*/M_\odot) \gtrsim 8.5$ due to sensitivity limits.

The more typical star-forming galaxies ($H\beta + [\text{O III}] \lesssim 230$ Å) at $3 < z_{\text{spec}} < 3.8$ have larger stellar masses ($\log(M_*/M_\odot) \gtrsim 10$) and lower rest-frame [O III]5007 Å equivalent widths ($EW_{\text{rest}} \sim 40$ – 250 Å; Figure 3). This reflects the larger contribution of stellar continuum light, i.e., for two galaxies with the same [O III]5007 Å line flux, the galaxy with the brighter continuum will have a lower equivalent width. Our results confirm that selecting SELGs from the ZFOURGE photometry is effective at identifying galaxies with the largest [O III]5007 Å equivalent widths.

For the S_1 ELG, the [O III]5007 Å EW_{rest} values determined using the line fluxes obtained with MOSFIRE (see Section 2.2.4) tend to be lower than the EW_{rest} value estimated from the composite SED (Figure 3). The offset is likely driven by how the continuum and emission lines are combined to generate the template used to fit the composite SEDs. For example, underestimating the continuum will increase the inferred EW. We refer the reader to Forrest et al. (2017), who test three fitting methods on the composite SEDs of the strongest ELGs.

3.2. Rest-frame UVJ Colors

With the ZFOURGE rest-frame wavelength coverage of 0.08– $7 \mu\text{m}$ for each galaxy, we measure continuum properties including rest-frame UVJ colors from the individual SEDs (Tomczak et al. 2014; Straatman et al. 2016). ZFOURGE galaxies at $2.5 < z_{\text{phot}} < 4.0$ span the range in UVJ colors (Figure 4) to include dusty and quiescent systems, but most lie in the star-forming region of the UVJ diagram (see also Straatman et al. 2016). The “typical” star-forming galaxies in our spectroscopic sample have $(V - J) \lesssim 0.5$ that are values consistent with low amounts of reddening ($A_V < 0.5$; Forrest et al. 2016). None of the spectroscopically confirmed galaxies are dusty as defined using the criterion from Spitler et al. (2014) of $(V - J) \geq 1.2$.

In contrast, the SELGs are offset toward bluer $(V - J)$ colors (Figure 4). Their strong $H\beta + [\text{O III}]$ emission significantly boosts their V -band fluxes to produce rest-frame values of $(V - J) < 0$; this is particularly striking for the S_1 ELG, where virtually all have $(V - J) < 0$. Such blue UVJ colors and nondetections in the far-IR indicate that these ELGs are essentially dust-free systems. The relative distributions of the S_1 ELG and S_2 ELG in the UVJ diagram suggests a continuum of phases where age and dust content increases from the SELGs to the more typical star-forming galaxies, e.g., Lyman-break galaxies.

3.3. Star Formation Rate versus Stellar Mass

SELGs tend to be lower-mass systems [$\log(M_*/M_\odot) \sim 8.2$ – 9.6] compared to more typical star-forming galaxies (Figure 3). At $z \sim 3$, the $\log(M^*)$ for the stellar luminosity

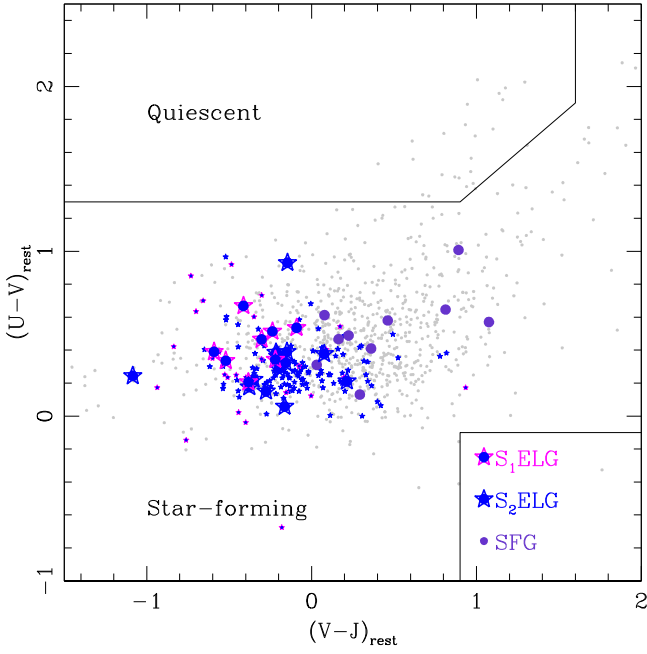


Figure 4. Rest-frame UVJ colors of ZFOURGE galaxies at $2.5 < z_{\text{phot}} < 4.0$ identified using Composite SEDs, i.e., with photometry only (Forrest et al. 2017). The SELGs are galaxies from the two composite SEDs with the strongest blended $H\beta + [\text{O III}]$ emission ($S_1\text{ELG}$ and $S_2\text{ELG}$; small stars). Larger symbols show the 31 spectroscopically confirmed galaxies at $3 < z_{\text{spec}} < 3.8$ that include more typical star-forming galaxies (purple). Typical uncertainties in rest-frame colors are not significant (< 0.1), i.e., comparable with the symbol sizes. Because of their strong $H\beta + [\text{O III}]$ emission, SELGs (stars) tend to have $(V - J) < 0$ colors and are offset relative to the broader ZFOURGE population at $2.5 < z_{\text{phot}} < 4.0$ (gray circles). None of the MOSEL galaxies are dusty as defined using the criterion from Spitler et al. (2014) of $(V - J) \geq 1.2$.

function from ZFOURGE is ~ 10.7 (Tomczak et al. 2014). In comparison, the SELGs have stellar masses of only $M_* \sim (0.003\text{--}0.08) M_\odot$.

Figure 5 shows the star formation rate to stellar mass ($\text{SFR}-M_*$) for the galaxies in our sample with measured (UV+IR) star formation rates from ZFOURGE (Tomczak et al. 2016). Although all of our galaxies have measured UV fluxes, many have negative IR fluxes due to the SED-fitting method (see Section 2.5 of Tomczak et al. 2016), thus 13 of the 31 galaxies have negative (unphysical) total SFRs and are excluded from the $\text{SFR}-M_*$ analysis. Also, note that our 3σ line-flux limit in the MOSFIRE K -band is $\sim 3 \times 10^{-18} \text{ erg s}^{-1} \text{ cm}^{-2}$ (see also Tran et al. 2017).

Of the 18 ELGs with positive (UV+IR) SFRs, all lie above the relation between star formation and stellar mass commonly referred to as the star-forming main sequence (SFMS; Figures 5 and 6); we confirm this is true even if we include UV only SFRs. The ELGs tend to lie ~ 0.9 dex above the SFMS at $z = 3.5$ as measured by Tomczak et al. (2016) from stacked SFRs based on (UV+IR) fluxes from ZFOURGE. The overall distribution of the spectroscopically confirmed SELGs mirrors that of the photometrically selected sample at this epoch, i.e., most of the SELGs lie above the SFMS.

With stellar mass-doubling timescales of only $\sim 10\text{--}100$ Myr, virtually all of the SELGs are starbursts (Figures 5 and 6). Our results are consistent with Amorín et al. (2017) and Maseda et al. (2014), who find that SELGs at $1 < z < 3$ have elevated SFRs for their given stellar mass. At stellar masses of $\log(M_*/M_\odot) \sim 9\text{--}9.5$, where the two redshift samples overlap, our SELGs at $2.5 < z_{\text{phot}} < 4.0$ have higher SFRs compared to the $z \sim 2$

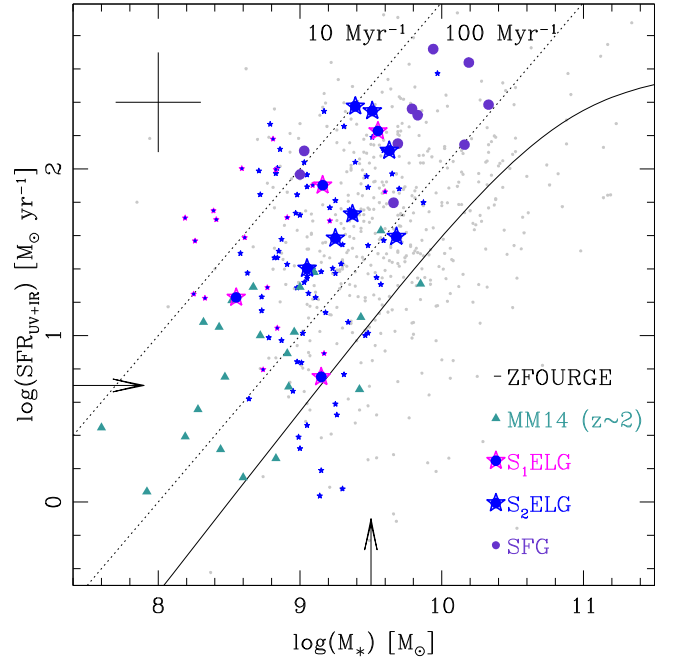


Figure 5. $H\beta + [\text{O III}]$ emitting galaxies tend to lie ~ 0.9 dex above the star-forming main sequence (SFMS) at $z = 3.5$ (solid curve based on stacked star formation rates; Tomczak et al. 2016); symbols are as in Figure 4 and the illustrative error bars correspond to a factor of two uncertainty in stellar mass and star formation rate. Arrows denote the completeness limits at $z \sim 3.5$ from ZFOURGE (Tomczak et al. 2016). Total star formation rates are based on ZFOURGE (UV+IR) fluxes, and here we plot only the galaxies that are individually detected in the IR. The Strong $H\beta + [\text{O III}]$ -emitters with z_{spec} (large stars) have the same distribution as their respective z_{phot} samples (small stars). The diagonal dotted lines denote mass-doubling timescales of 10 and 100 Myr. SELGs at $1.4 < z < 2.3$ (filled triangles; Maseda et al. 2014) also tend to lie above the SFMS.

SELGs. However, we note that for low-mass galaxies ($\log(M_*/M_\odot) \lesssim 10$), the observed scatter in M_* -SFR increases with increasing redshift (Tomczak et al. 2016).

A possible concern is that our (UV+IR) based SFRs are near or below the nominal IR detection limit at $z \sim 3.5$ (Tomczak et al. 2016). However, the very lack of IR emission is consistent with SELGs having little to no dust. We find additional support for the elevated SFRs and specific SFRs for the SELGs in Cohn et al. (2018): using the SED-fitting code *Prospector* (Conroy et al. 2009; Leja et al. 2017), Cohn et al. (2018) show that the SELGs with $H\beta + [\text{O III}]$ $\text{EW}_{\text{rest}} \gtrsim 800 \text{ \AA}$ ($S_1\text{ELG}$) are dominated by the current starburst and have rising star formation rates.

3.4. Galaxy Size versus Stellar Mass

Our ELGs lie on the galaxy size–mass ($r_{\text{eff}}-M_*$) relation measured by Allen et al. (2017) using ZFOURGE galaxies at $3 < z_{\text{phot}} < 3.75$ (Figure 7). Here we use the effective radii (galaxy size) measured by van der Wel et al. (2012) with the WFC3/F160W imaging and consider only galaxies with goodness of fit flag of 0. These criteria further reduce our ELG sample to 13 galaxies. We note that relaxing the goodness of fit flag to include all ELGs with measured r_{eff} (28) increases the scatter in the galaxy size–mass relation, but does not change the overall result.

Although they are virtually all starbursts (Figures 5 and 6), our ELGs at $2.5 < z_{\text{phot}} < 4.0$ follow the same $r_{\text{eff}}-M_*$ relation as the general population. The SELGs at $1 < z < 3$ (Maseda et al. 2014) are also consistent with the same size–mass relation, except for the lowest-mass systems ($\log(M_*/M_\odot) < 8.5$) that tend to lie below

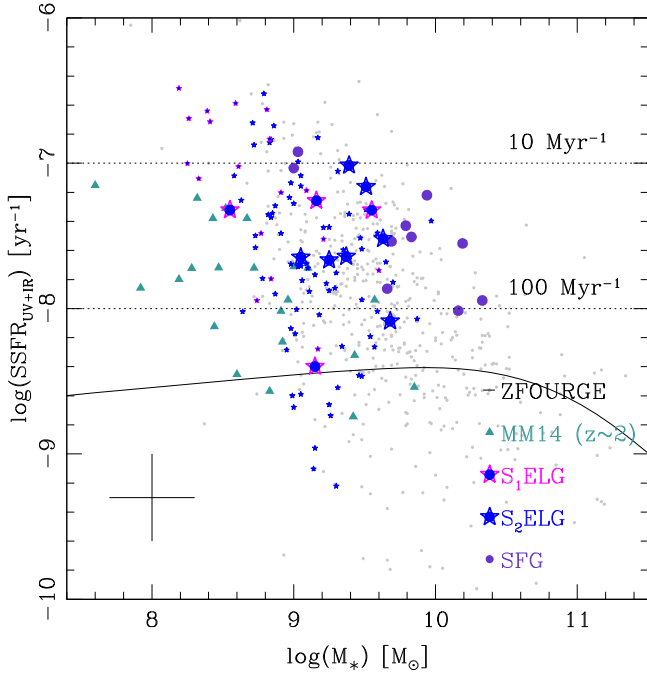


Figure 6. The starburst nature of the $H\beta$ + $[O\text{ III}]$ emitting galaxies is underlined by their high specific star formation rates (SSFR), defined as their (UV+IR) SFRs divided by their stellar masses. Symbols are as in Figure 5 and included for comparison is the SSFR- M_* at $z = 3.5$ from Tomczak et al. (2016); illustrative error bars correspond to a factor of two uncertainty in stellar mass and specific star formation rate. Most of the SELGs (stars) have mass-doubling times of <100 Myr, with several systems at <10 Myr (dotted horizontal lines). Included for comparison are the ELGs at $1 < z < 3$ from Maseda et al. (2014) that all have mass-doubling times >10 Myr and tend to be low mass ($\log(M_*/M_\odot) < 9$). As SELGs grow in stellar mass and evolve into more typical SFGs, they move diagonally from the upper left to the bottom right.

this relation, i.e., they are more compact at a given stellar mass. Combining both redshift samples suggests that the SELGs are an early phase in the continuum of stellar growth.

3.5. Inferred Gas Fractions

With UV+IR luminosities from ZFOURGE and r_{eff} from the HST/F160W imaging (van der Wel et al. 2012), we use the Schmidt–Kennicutt Relation (SKR; Schmidt 1959; Kennicutt 1998, Equation (7)) to estimate the gas surface density for individual galaxies:

$$\Sigma_{\text{SFR}} = (2.5 \pm 0.7) \times 10^{-4} \times \left(\frac{\Sigma_{\text{gas}}}{1M_\odot \text{ pc}^{-2}} \right)^{1.4 \pm 0.15} M_\odot \text{ yr}^{-1} \text{ kpc}^{-2}. \quad (2)$$

Assuming that half of the gas mass is within r_{eff} , we use Σ_{SFR} to estimate the total gas mass:

$$\log(M_{\text{gas}}) = \frac{5}{7} \log(L_{\text{UV+IR}}) + \frac{2}{7} \log[\pi(r_{\text{eff}})^2] + 1.52, \quad (3)$$

where r_{eff} is measured in kpc, M_{gas} in M_\odot , and $L_{\text{UV+IR}}$ in L_\odot ; see also Papovich et al. (2015). We use r_{eff} defined by the stellar light; note that studies using CO (Tacconi et al. 2013) and $H\alpha$ (Förster Schreiber et al. 2011) find r_{eff} from gas and stars are consistent. Assuming an observational detection limit of $L_{\text{UV+IR}} = 10^{11} L_\odot$

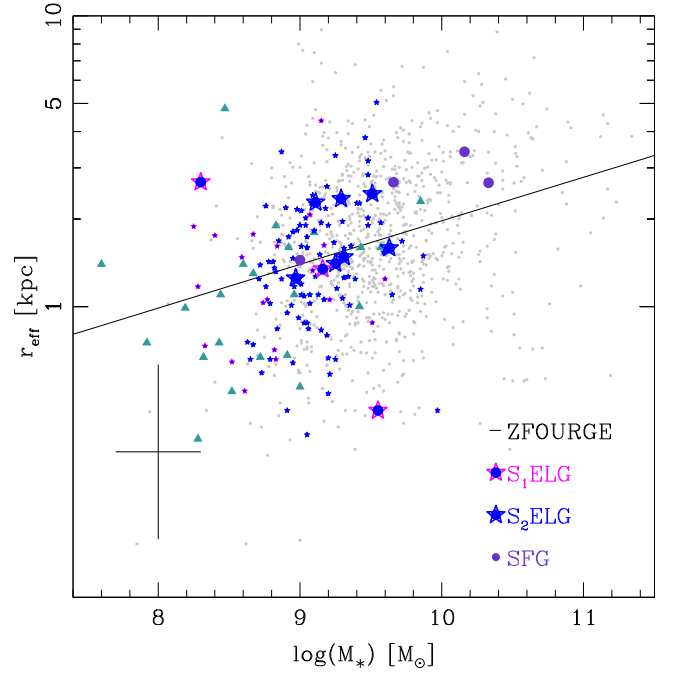


Figure 7. The $H\beta$ + $[O\text{ III}]$ emitters are consistent with the ZFOURGE galaxy size-stellar mass relation at $3 < z_{\text{phot}} < 3.75$ from Allen et al. (2017) (solid line), but there is considerable scatter both in the ELGs and for all ZFOURGE galaxies at $2.5 < z_{\text{phot}} < 4.0$. Here we use the effective radii measured by van der Wel et al. (2012) with WFC3/F160W imaging and the symbols are as in Figure 5. The illustrative error bars correspond to a factor of two uncertainty in stellar mass and galaxy size. The SELGs at $z \sim 2$ (filled triangles; Maseda et al. 2014) are consistent with the same mass-size relation except at the lowest mass ($\log(M_*/M_\odot) < 8.5$), where they tend to be more compact.

and typical galaxy size of $r_{\text{eff}} = 3.2$ kpc (Tran et al. 2017), the corresponding gas mass limit is $\log(M_{\text{gas}}/M_\odot) = 9.8$. Gas fractions are defined to be $M_{\text{gas}}/(M_{\text{gas}}+M_*)$.

All of our spectroscopically confirmed ELGs have inferred gas fractions of $f_{\text{gas}} > 60\%$ (Figure 8), which is not surprising given the ELGs’ high specific star formation rates and our detection limits. The high gas masses are consistent with high accretion rates that may be driving the star formation (Kacprzak et al. 2016). Our inferred gas fractions combined with measurements of SELGs at $z \sim 2$ (Maseda et al. 2014) suggests that $f_{\text{gas}} \gtrsim 80\%$ for ELGs with stellar masses of $\log(M_*/M_\odot) < 9$. However, direct measurements of gas masses for the ELGs at $z > 2$ with stellar masses of $\log(M_*/M_\odot) < 9$ will be difficult given current observational limitations.

3.6. Kinematics

The integrated velocity dispersions (σ_{int}) based on $[O\text{ III}]$ 5007 Å line widths is $\sigma_{\text{int}} \sim 40\text{--}150 \text{ km s}^{-1}$ for most of the ELGs with only one ELG having $\sigma_{\text{int}} \sim 200 \text{ km s}^{-1}$ (see Tables 1 and 2). Combining σ_{int} and effective radii from vdW12, we follow Alcorn et al. (2016) and estimate virial masses:

$$M_{\text{dyn}}(<R_e) = K_e \frac{\sigma_{\text{int}}^2 R_e}{G}, \quad (4)$$

where for consistency with Maseda et al. (2013, 2014), we adopt the virial factor $K_e = 3$ that is typically used for disk galaxies.

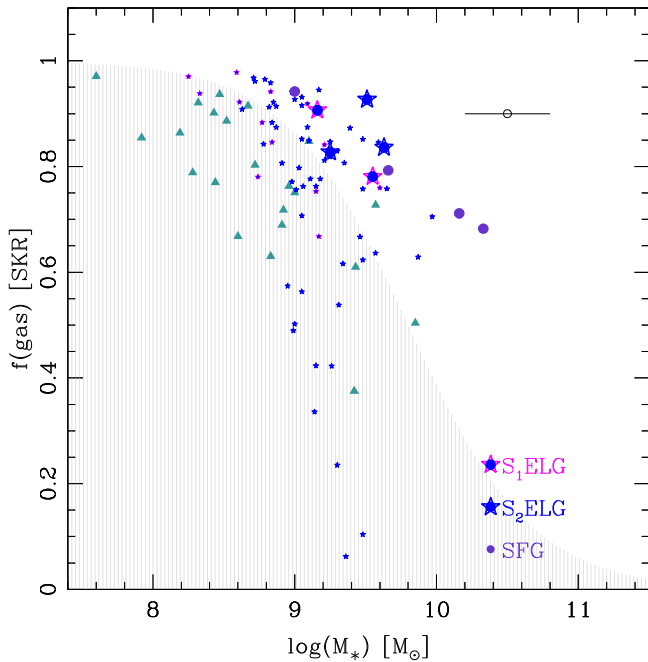


Figure 8. We infer gas masses by using the Schmidt–Kennicutt Relation (SKR; Kennicutt 1998) with effective sizes from vdW12 and total luminosities from Tomczak et al. (2016); symbols are as in Figures 4 and 5. The illustrative error bars correspond to a factor of two uncertainty in stellar mass and we note that the gas mass is highly uncertain. For reference, we show the exclusion region corresponding to a gas mass limit of $\log(M_*/M_\odot) = 9.8$ (light gray shaded region) which is below our nominal detection threshold at $z \gtrsim 3$. All of the spectroscopically confirmed ELGs in our study have inferred gas mass fractions of $f_{\text{gas}} > 60\%$, but this is expected given the combination of their high specific star formation rates (see Figure 6) and our detection limits at $z \sim 3.5$. The SELGs will move to the right as they increase in stellar mass and, unless their gas reservoirs are replenished, downward.

The dynamical masses for our ELGs at $3 < z_{\text{spec}} < 3.8$ are ~ 0.4 dex larger than their stellar masses (Figure 9); the handful of galaxies with $M_{\text{dyn}} < M_*$ is consistent with scatter due to errors in the measurements. The offset between virial and stellar mass is consistent with measurements of SELGs at $z \sim 2$ (Maseda et al. 2013, 2014) and continues the same trend to higher masses. Within our limited sample at $3 < z_{\text{spec}} < 3.8$, there is no obvious difference in the M_* – M_{dyn} relation for SELGs compared with higher mass ($\log(M_*/M_\odot) > 9$) star-forming galaxies.

When comparing the total baryonic mass (sum of the stellar and estimated gas mass) with dynamical mass, we find that the MOSEL galaxies are closer to parity (Figure 9, left). However, given the scatter and low number statistics, we hesitate to draw any stronger conclusions regarding the ratio of dark to baryonic mass for the MOSEL galaxies.

3.7. Star Formation or Active Galactic Nuclei?

Our analysis assumes that the strong [O III]5007 Å emission is driven by star formation and not AGNs. We have used the ZFOURGE catalog by Cowley et al. (2016) to remove AGNs but recognize that at $z > 3$, the multiwavelength AGN diagnostics may not be reliable, especially given the uneven coverage across these fields. However, the [O III]5007 Å line widths are consistent with star formation: most of the ELGs have $\sigma_{\text{int}} \sim 40$ – 150 km s^{-1} with only one ELG having $\sigma_{\text{int}} \sim 200 \text{ km s}^{-1}$ (see Tables 1 and 2). Also, our recent results using Prospector to construct the star formation histories of

the SELGs confirms that they are dominated by starbursts spanning the most recent ~ 50 Myr (Cohn et al. 2018). Last, we note that AGN contamination is rare in low-mass galaxies (e.g., Ho et al. 1997; Trump et al. 2015).

Unlike the ZFOURGE composite SEDs where $H\beta$ and [O III]5007 Å are blended (Forrest et al. 2017), the MOSFIRE spectroscopy easily resolves these spectral features for individual ELGs. Thus, we also can identify potential AGNs by combining the ratio of [O III]5007 Å to $H\beta$ with stellar mass (Juneau et al. 2011), although we note this method is contested at $z > 1$ (Trump et al. 2013). The median [O III]5007/ $H\beta$ value for our sample of ELGs is ~ 5.8 , which is consistent with values reported by (Holden et al. 2016) for Lyman-break galaxies at $z \sim 3$. Following a similar line of analysis, Maseda et al. (2014) also excluded AGNs from their sample of SELGs at $1 < z < 2$.

$H\beta$ is weaker than [O III]5007 Å, and given our line-flux limit of $\sim 3 \times 10^{-18} \text{ erg s}^{-1} \text{ cm}^{-2}$ (3σ), we can only place upper limits on the ratio of [O III]5007/ $H\beta$ for many of the ELGs. A more careful treatment of the $H\beta$ line fluxes, e.g., by stacking the spectra, can be used to constrain ISM conditions. Further analysis that includes $H\beta$, e.g., by combining [O III]5007/ $H\beta$ with stellar masses and star formation histories, will be presented in a future MOSEL paper.

4. Discussion

With deep multiband photometry from ZFOURGE, we identified ELGs at $z > 2.5$ that have blended rest-frame $H\beta$ + [O III] equivalent widths of $\gtrsim 230$ Å (Forrest et al. 2017, 2018). We consider the combined sample of SELGs grouped in the two composite SEDs with the largest $H\beta$ + [O III] equivalent widths ($\text{EW}_{\text{rest}} > 230$ Å; see Section 2.1.2). The rarity of ELGs with $\text{EW}_{\text{rest}}([\text{O III}]5007) \gtrsim 200$ Å in the local universe (~ 2 “green peas” per square degree; Cardamone et al. 2009) raises the question of whether this strong emission-line phase is the exception or the norm at high redshifts. In our MOSEL survey, we build on recent studies to further explore how galaxies at $z \sim 3.5$ with strong [O III]5007 Å emission fit into our current understanding of how star-forming galaxies grow by combining Keck/MOSFIRE K -band spectroscopy with our existing multiband photometry from ZFOURGE.

4.1. Strong [O III]5007 Å Emission May Be Common in Early Galaxy Formation

We spectroscopically confirm 31 galaxies at $3 < z_{\text{spec}} < 3.8$ with stellar masses of $\log(M_*/M_\odot) \sim 8.2$ – 10.2 and rest-frame [O III]5007 Å equivalent widths up to ~ 500 Å (Figures 1 and 3). The properties of the spectroscopically confirmed SELGs mirror that of the larger photometrically selected sample (e.g., Figures 4 and 5). Most of the SELGs have blue colors of $(V - J) < 0$ while the more typical star-forming galaxies have $(V - J) \sim 0$ – 1 (Figure 4). The overlapping ranges in their rest-frame UVJ colors suggest that the SELGs transition into more massive star-forming galaxies, e.g., Lyman-break galaxies.

In the stellar mass range where we overlap with MOSDEF galaxies at $z \sim 2$ (Reddy et al. 2018), we find a similar relationship between [O III]5007 Å EW_{rest} and stellar mass (Figure 3). Reddy et al. (2018) suggest that the increasing [O III]5007 Å EW_{rest} with decreasing stellar mass can be explained by either rapid enrichment of α elements or metallicities of $\lesssim 0.2Z_\odot$ for galaxies with $\log(M_*/M_\odot) \lesssim 9$.

Table 1
MOSEL Galaxy Properties^a

Field	ZFOURGE ^b ID	R.A. ^b J2000	Decl. ^b J2000	z_{spec} ± 0.003	z_{phot} ± 0.0135	K_{obs} ^b mag	$(U - V)^b$ mag	$(V - J)^b$ mag	$\log(M_*/M_\odot)^c$	$\log(\text{SFR})^c$ $M_\odot \text{ yr}^{-1}$	r_{eff}^d kpc
COSMOS	1877	150.170425	2.199359	3.1230	3.16	22.92	0.58	0.46	10.2	2.1	3.4
COSMOS	4214	150.177109	2.221284	3.4578	3.38	23.39	1.01	0.89	10.3	2.4	2.7
COSMOS	7239	150.202240	2.254340	3.1198	3.18	23.85	0.24	-1.08	9.0	<1	0.7
COSMOS	9884	150.072495	2.282637	3.2982	3.39	23.42	0.93	-0.15	9.1	1.4	1.4
COSMOS	11063	150.146133	2.297038	3.0393	3.04	23.63	0.34	-0.22	8.9	<1	1.8
COSMOS	11284	150.136337	2.298915	3.3016	3.47	23.09	0.32	-0.16	9.4	1.7	2.4
COSMOS	11544	150.147446	2.301592	3.3038	3.36	22.86	0.29	-0.20	9.5	2.3	2.4
COSMOS	12000	150.070665	2.305136	3.2578	3.28	22.88	0.65	0.81	10.2	2.6	...
COSMOS	12105	150.138840	2.306907	3.2976	3.41	23.25	0.54	-0.09	9.2	1.9	1.3
COSMOS	12273	150.147030	2.309289	3.1809	3.29	23.39	0.31	0.03	9.8	2.4	...
COSMOS	12776	150.121275	2.315327	3.4993	3.55	23.69	0.57	1.08	9.8	2.3	...
COSMOS	12922	150.069214	2.315987	3.2556	3.35	23.24	0.47	0.16	9.7	1.8	2.7
COSMOS	14984	150.060333	2.338560	3.3777	3.50	23.29	0.18	-0.38	9.3	<1	1.5
COSMOS	15625	150.139206	2.345322	3.1841	3.22	23.50	0.36	-0.20	9.2	1.6	1.4
COSMOS	15636	150.065445	2.345667	3.4188	3.51	24.21	0.13	0.29	9.0	2.0	1.4
COSMOS	16067	150.200134	2.349396	3.1885	3.21	22.89	0.47	-0.30	9.2	<1	1.4
COSMOS	16325	150.203055	2.352349	3.4538	3.55	23.40	0.49	0.22	9.7	2.2	...
COSMOS	16513	150.066735	2.353337	3.4188	3.49	22.89	0.22	-0.35	9.2	<1	...
COSMOS	16518	150.211500	2.354372	3.3653	3.14	23.47	0.41	0.36	9.9	2.7	...
COSMOS	16984	150.083664	2.358806	3.3273	3.44	23.11	0.38	0.08	9.3	<1	2.3
COSMOS	17008	150.168793	2.358994	3.4608	3.55	23.76	0.21	0.21	9.0	<1	1.3
COSMOS	17423	150.115402	2.363473	3.5259	3.55	23.95	0.51	-0.24	9.6	2.2	0.4
COSMOS	17909	150.094330	2.370171	3.1977	3.49	22.58	0.39	-0.15	9.6	2.1	1.6
COSMOS	18022	150.079529	2.367794	3.4188	3.48	23.89	0.15	-0.28	9.1	<1	2.3
COSMOS	20001	150.214305	2.378608	3.4488	3.54	22.93	0.39	-0.22	9.4	2.4	...
CDFS	22136	53.152866	-27.749243	3.0883	3.19	22.93	0.34	-0.52	9.2	0.8	1.6
CDFS	15782	53.174133	-27.800318	3.0651	3.15	24.30	0.61	0.08	9.0	2.1	0.2
CDFS	18053	53.195736	-27.782713	3.3239	3.31	24.73	0.21	-0.38	8.6	1.2	0.4
CDFS	17189	53.198280	-27.789150	3.5506	3.54	24.73	0.39	-0.59	8.3	<1	2.7
CDFS	14864	53.204610	-27.806757	3.5552	3.47	22.52	0.06	-0.16	9.7	1.6	...
CDFS	15561	53.219540	-27.802586	3.0865	3.03	24.68	0.67	-0.41	8.9	<1	0.4

Notes.

^a We include only MOSEL galaxies with spectroscopic redshift quality flag of $Q_z \geq 2.5$ (see Tran et al. 2015; Nanayakkara et al. 2016).

^b Galaxy identification numbers, observed ZFOURGE K -band magnitudes, photometric redshifts, and rest-frame UVJ are from ZFOURGE (Straatman et al. 2016). Uncertainties on the magnitudes and colors are < 0.01 .

^c We use the stellar masses from Forrest et al. (2018) and the combined UV+IR star formation rates from Tomczak et al. (2016). We recommend the reader considers a typical uncertainty of ~ 0.3 dex for both parameters.

^d Effective radii are from van der Wel et al. (2012) and measured using the WFC3/F160W imaging. Here we take the sizes reported in arcsec and convert to kpc using the angular diameter distance.

Both scenarios are consistent with our interpretation that the SELGs are young and have subsolar metallicities.

In combination with Cohn et al. (2018), who show that SELGs at $z \sim 3.5$ have low gas-phase metallicities ($Z_* \lesssim 0.02Z_\odot$) and higher specific star formation rates relative to SFGs (4.6 Gyr^{-1} versus 1.1 Gyr^{-1}), our spectroscopic measurements support a scenario where strong [O III]5007 Å emission signals the earliest episodes of intense star formation (see also Amorín et al. 2017). As the SELGs grow in stellar mass, the growing amount of continuum light means that even during subsequent episodes of bursty star formation, the [O III]5007 Å equivalent widths will not be as large as during the first major burst of star formation. With star formation rates of $\gtrsim 3\text{--}250 M_\odot \text{ yr}^{-1}$ (Figure 5) and mass-doubling times of $\sim 10\text{--}100 \text{ Myr}$ (Figures 5 and 6), the intense [O III]5007 Å emission phase is brief as these same galaxies quickly transition into more typical star-forming galaxies with $H\beta + [\text{O III}] \text{ EW}_{\text{rest}} \lesssim 230 \text{ \AA}$.

We find further support for a picture where strong [O III] 5007 Å emission signals the earliest stages of stellar growth in

galaxies by comparing relations between stellar mass (M_*), galaxy size (r_{eff}), and virial mass (M_{dyn}). Our SELGs follow the same general $M_*\text{--}r_{\text{eff}}$ relation as that of star-forming galaxies at $z \sim 3$ (Figure 7), although we note the large scatter for all galaxies at this epoch. The SELGs also continue the same trend between $M_{\text{dyn}}\text{--}M_*$, as measured for SELGs at $z \sim 2$ (Figure 9). The SELGs have virial masses that are larger by ~ 0.4 dex relative to their stellar masses which is consistent with their inferred gas mass fractions of $f_{\text{gas}} > 60\%$ (Figure 8).

In a recent paper (Cohn et al. 2018), we derived galaxy properties from the ZFOURGE photometry using the SED-fitting code *Prospector* (Leja et al. 2017) and the Flexible Stellar Population Synthesis package (FSPS; Conroy et al. 2009). The *Prospector* code finds the best-fit model and estimates uncertainties by sampling the posterior probability distributions of all the free parameters. By calculating nonparametric star formation histories, *Prospector* can distinguish between rising, falling, and bursty star formation histories.

Table 2
MOSEL: [O III]5007 Å Properties

Field	ZFOURGE ^a ID	$f(5007 \text{ \AA})^b$ $10^{-17} \text{ erg s}^{-1} \text{ cm}^{-2}$	σ_{D}^b Å	σ_{int}^b km s^{-1}	$\text{EW}_{\text{rest}}^c$ Å
COSMOS	1877	2.2 ± 0.6	10.5	151	23.3
COSMOS	4214	1.4 ± 1.1	3.0	39	23.0
COSMOS	7239	10.1 ± 0.3	4.3	62	542
COSMOS	9884	10.5 ± 0.6	9.0	124	392
COSMOS	11063	17.3 ± 0.4	4.1	60	468
COSMOS	11284	16.8 ± 0.9	4.9	68	262
COSMOS	11544	12.3 ± 0.6	6.0	83	153
COSMOS	12000	8.3 ± 0.4	8.5	119	78.0
COSMOS	12105	9.6 ± 0.7	4.9	67	221
COSMOS	12273	8.0 ± 0.5	7.7	110	78.6
COSMOS	12776	11.5 ± 1.6	8.7	116	199
COSMOS	12922	4.9 ± 1.1	10.0	141	67.6
COSMOS	14984	8.1 ± 0.2	5.1	70	228
COSMOS	15625	8.7 ± 0.3	4.1	58	199
COSMOS	15636	4.8 ± 0.5	11.4	154	514
COSMOS	16067	24.8 ± 0.4	6.3	90	428
COSMOS	16325	6.7 ± 1.3	7.8	105	109
COSMOS	16513	13.0 ± 0.6	4.3	58	289
COSMOS	16518	4.3 ± 1.0	8.3	113	40.8
COSMOS	16984	14.7 ± 0.3	4.4	60	405
COSMOS	17008	10.6 ± 0.8	6.3	84	399
COSMOS	17423	12.3 ± 1.1	6.9	90	285
COSMOS	17909	22.5 ± 0.7	8.8	125	248
COSMOS	18022	6.5 ± 0.4	6.2	83	282
COSMOS	20001	22.0 ± 0.5	7.3	97	378
CDFS	22136	2.8 ± 0.7	14.3	208	97.0
CDFS	15782	2.6 ± 0.5	6.6	96	240
CDFS	18053	1.0 ± 0.6	3.6	49	165
CDFS	17189	2.3 ± 0.4	8.0	105	506
CDFS	14864	2.7 ± 0.3	10.8	142	46.6
CDFS	15561	3.2 ± 0.2	2.8	41	430

Notes.

^a Galaxy identification numbers are from ZFOURGE (Straatman et al. 2016).

^b [O III]5007 Å line flux, line width (σ_{D}), and the corresponding integrated velocity dispersion (σ_{int}) are measured by fitting a Gaussian to the MOSFIRE spectra (see Section 2.2.3).

^c [O III]5007 Å rest-frame equivalent widths are determined using the line flux measured with MOSFIRE spectroscopy and continuum flux from the best-fit FAST SED (see Section 2.2.4).

Using Prospector, Cohn et al. (2018) show that ELGs with extreme emission ($S_1\text{ELG}$; $H\beta + [\text{O III}] \text{EW}_{\text{rest}} \gtrsim 800 \text{ \AA}$) are “first burst” systems and are likely to have rising star formation rates. These same galaxies have low gas-phase metallicities of $Z_* \lesssim 0.02Z_\odot$ and higher specific star formation rates compared to star-forming galaxies: $\sim 4.6 \text{ Gyr}^{-1}$ versus $\sim 1.1 \text{ Gyr}^{-1}$. Cohn et al. (2018) inferred that many, if not most, star-forming galaxies at $z > 2.5$ have Extreme $H\beta + [\text{O III}]$ emission-line phases early in their formation histories. As these “first burst” systems continue to form stars and chemically enrich to evolve into more typical SFGs, they move diagonally from the upper left to the bottom right in Figures 6 and 8.

4.2. A Potential Source of Ionizing UV Photons

A growing number of studies indicate that galaxies rather than AGNs generated the UV photons needed to ionize the universe, but there are not enough massive galaxies at $z \gtrsim 6$ to generate the required UV photons (Robertson et al. 2013, 2015). With several low-mass ($\log(M_*/M_\odot) \lesssim 9$) systems now identified at $z > 3$ that have strong $\text{EW}_{\text{rest}}([\text{O III}]5007) > 300 \text{ \AA}$ and escape fractions of $f_{\text{esc}} \gtrsim 10\%$ (de Barros et al. 2016; Nakajima et al. 2016), the

most viable source of UV photons are these low-mass, star-bursting galaxies. However, the stellar mass function at $z > 8$ must be steeper than observed at lower redshifts for there to be enough of these dwarf galaxies to generate the required UV photons.

Another potential source of UV photons are the galaxies in our study with $\text{EW}_{\text{rest}}([\text{O III}]5007) > 200 \text{ \AA}$, e.g. galaxies in a strong emission-line phase. The inferred gas fractions of $f_{\text{gas}} \gtrsim 60\%$ (Figure 8) and high specific star formation rates (Figure 6) imply that the ELGs with the strongest [O III]5007 Å easily increase their stellar masses by factors > 2 in less than $\sim 100 \text{ Myr}$, i.e., these SELGs signal the earliest stages of stellar growth in galaxies (see also Cohn et al. 2018).

If the [O III]5007 Å emitters also have large [O III]5007/[O II]3727 ratios ($\text{O}32 \gtrsim 5$), studies indicate they may leak more Lyman-continuum photons due to their harder ionizing spectrum (Nakajima & Ouchi 2014; Izotov et al. 2016; Nakajima et al. 2016). Tang et al. (2019) find that in the most intense line emitters at $z \sim 2$, the ionizing photon efficiency scales with [O III]5007 Å emission. However, recent results by Bassett et al. (2019) of galaxies at $z \sim 3$ suggest that the correlation between large [O III]5007/[O II]3727 ratios and

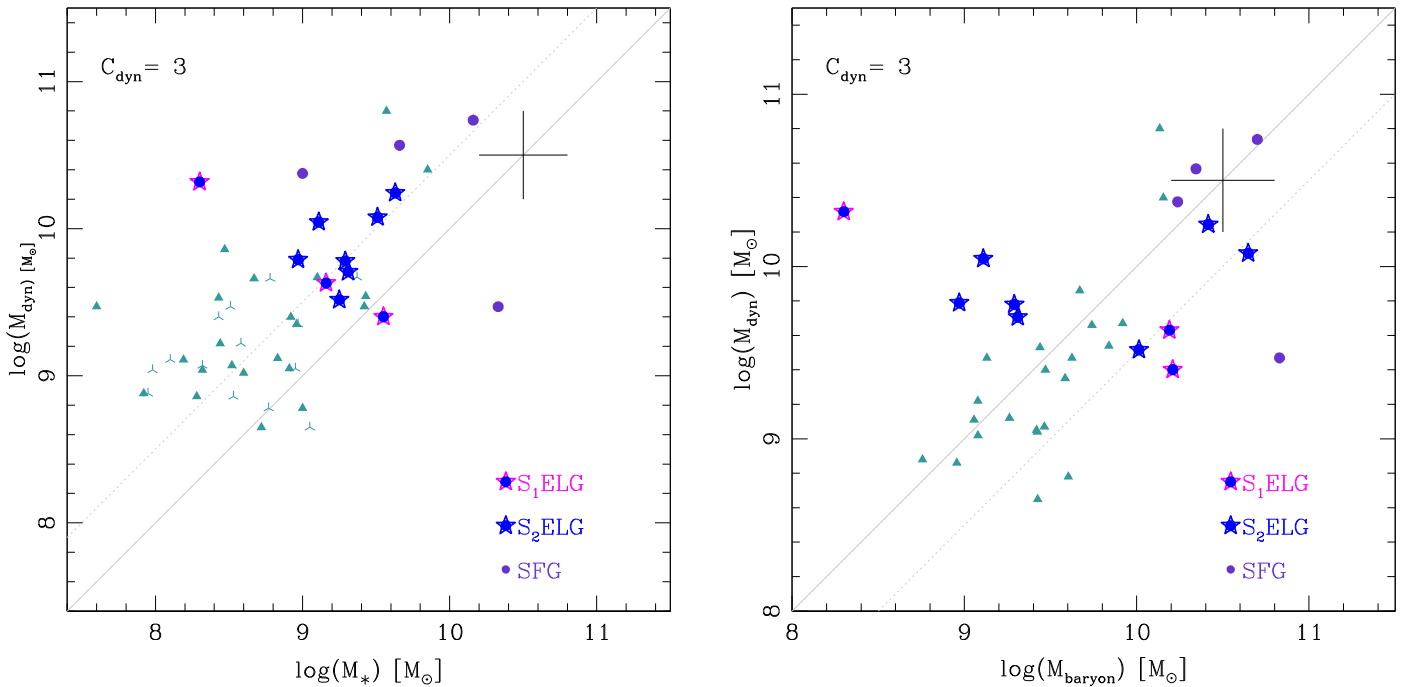


Figure 9. Left: the dynamical masses for the [O III]5007 Å emitting galaxies at $3 < z_{\text{spec}} < 3.8$ are ~ 0.4 dex larger than their stellar masses (symbols are as in Figure 3). The illustrative error bars correspond to a factor of two uncertainty in mass. We estimate virial masses by combining the [O III]5007 Å line widths with effective radii measured by vdW12 (see Alcorn et al. 2016, 2018). The solid diagonal line is parity, and the dotted line is offset by 0.5 dex. Our results are consistent with studies showing that ELGs at $z \sim 2$ tend to have $M_{\text{dyn}} > M_*$ (Maseda et al. 2013, 2014) and with their inferred gas mass fractions of $f_{\text{gas}} > 60\%$. Right: the same MOSEL galaxies where we now compare the total baryonic mass (the sum of the stellar and estimated gas mass) to their dynamical mass. Including f_{gas} brings the MOSEL galaxies closer to parity, but we hesitate to draw any stronger conclusions given the scatter and low number statistics.

more Ly-C photons is weak at best, and Naidu et al. (2018) constrain the average escape fractions for SELGs to be 8.5%–16.7%.

Only with spectroscopy can we measure fluxes of oxygen lines for individual galaxies to measure their ratios and determine what drives the strong [O III]5007 emission, e.g., shocks or massive binary stars (Strom et al. 2017). By obtaining at $z \sim 3.5$ the ratio of [O III]5007 to well-studied emission lines such as [O II]3727, $H\beta$, and $\text{Ly}\alpha$ (e.g., Bassett et al. 2019; Tang et al. 2019), we can better track how the ionizing photon efficiency evolves from the first galaxies to $z \sim 0$. We plan to measure [O II]3727 Å emission for our ELGs to characterize their ionization conditions and constrain their production of Lyman-continuum photons.

5. Conclusions

Our Multi-Object Spectroscopic Emission Line (MOSEL) survey focuses on galaxies with strong [O III]5007 Å emission identified using deep broadband photometry from the ZFOURGE survey (Forrest et al. 2017, 2018). We use Keck/MOSFIRE K -band spectroscopy and measure redshifts of 49 galaxies at $2.091 < z_{\text{spec}} < 4.751$. Our spectroscopic success rate is $\sim 53\%$ and z_{phot} uncertainty is $\sigma_z = [\Delta z / (1+z)] = 0.0135$ (Section 2.2.2, Figure 1; see also Nanayakkara et al. 2016; Straatman et al. 2016).

Of the 49 spectroscopically confirmed galaxies at $2.091 < z_{\text{spec}} < 4.751$, we measure [O III]5007 Å line fluxes for 31 galaxies at $3 < z_{\text{spec}} < 3.8$ (Figure 2). By dividing the line flux as measured with MOSFIRE by the continuum flux from ZFOURGE, we estimate rest-frame [O III]5007 Å equivalent widths of ~ 100 – 500 Å where EW_{rest} increases with decreasing stellar mass (Figure 3). Our analysis focuses on

the SELGs grouped in the two composite SEDs with the strongest $H\beta + [\text{O III}]$ emission ($\text{EW}_{\text{rest}} > 230\text{Å}$) from Forrest et al. (2018).

We explore the properties of SELGs at $z \sim 3.5$ to connect them to our current picture of star-forming galaxies. The physical properties of the spectroscopically confirmed [O III] 5007 Å SELGs mirror that of the larger photometrically selected sample. For example, the SELGs tend to have bluer colors of $(V - J) < 0$ compared to more typical star-forming galaxies with $(V - J) \sim 0$ – 1 (Figure 4).

The strong $H\beta + [\text{O III}]$ emitting galaxies in our study have stellar masses of $\log(M_*/M_\odot) \sim 8.2$ – 9.6 (Figure 5). The same galaxies lie ~ 0.9 dex above the star-forming main sequence at $z = 3.5$ and have high specific star formation rates with mass-doubling timescales of ~ 10 – 100 Myr (Figure 6). The inferred gas fractions of $f_{\text{gas}} \gtrsim 60\%$ (Figure 8) can easily fuel a burst that increases stellar mass by > 2 . In terms of stellar and virial mass, (UV+IR) star formation rate, and galaxy size, our $H\beta + [\text{O III}]$ emitting galaxies bridge relations measured for SELGs at $1 < z < 3$ ($\log(M_*/M_\odot) \lesssim 9$; van der Wel et al. 2011; Maseda et al. 2014) to star-forming galaxies at $z \sim 3.5$ (see Figures 5–7).

Taken as a whole, our analysis suggests that strong [O III] 5007 Å emission ($\text{EW}_{\text{rest}} \gtrsim 200$) signals an early episode of intense star formation in low-mass ($M_* < 0.1 M^*$) galaxies at $z \gtrsim 3$. The ELGs with the strongest [O III]5007 Å are a rapidly evolving population of galaxies both in number density and stellar growth (Forrest et al. 2017; Cohn et al. 2018). The [O III] 5007 Å ELGs are likely to evolve into more massive and older star-forming galaxies with stable disks and bulges, e.g., Lyman-break galaxies.

In a recent paper (Cohn et al. 2018), we estimated that many, if not most, star-forming galaxies at $z > 3$ are strong [O III] 5007 Å emitters early in their formation history. If strong [O III] 5007 Å emission is a common phase in early galaxy formation, this brief episode may generate a significant number of ionizing UV photons. In a future paper, we will explore additional line diagnostics, e.g., the ratio of [O III]5007 Å to $H\beta$, to characterize ionization conditions and constrain the production of Lyman-continuum photons in galaxies with the strongest [O III]5007 Å emission.

We are grateful to the Keck/MOSFIRE team, with special thanks to M. Kassis, J. Lyke, G. Wirth, and L. Rizzi on the Keck support staff. K. Tran thanks P. Oesch, B. Holden, and M. Maseda for helpful discussions, and B. Forrest thanks the Hagler Institute for Advanced Study at Texas A&M for support. We also thank the referee for a thoughtful and constructive report. This work was supported by a NASA Keck PI Data Award administered by the NASA Exoplanet Science Institute. Data presented herein were obtained at the W. M. Keck Observatory from telescope time allocated to NASA through the agency's scientific partnership with the California Institute of Technology and the University of California. The Observatory was made possible by the generous financial support of the W. M. Keck Foundation. K. Tran acknowledges that this material is based upon work supported by the National Science Foundation under grant No. 1410728 and acknowledges the ARC Centre for Excellence in All-Sky Astrophysics in 3D (ASTRO 3D) for support in preparing the manuscript. G. G.K. acknowledges the support of the Australian Research Council through the DP170103470. The authors wish to recognize and acknowledge the very significant cultural role and reverence that the summit of Maunakea has always had within the indigenous Hawaiian community. We are most fortunate to have the opportunity to conduct observations from this mountain.

ORCID iDs

Kim-Vy H. Tran  <https://orcid.org/0000-0001-9208-2143>
 Ben Forrest  <https://orcid.org/0000-0001-6003-0541>
 Leo Y. Alcorn  <https://orcid.org/0000-0002-2250-8687>
 Tiantian Yuan  <https://orcid.org/0000-0002-9211-3277>
 Themiyi Nanayakkara  <https://orcid.org/0000-0003-2804-0648>
 Jonathan Cohn  <https://orcid.org/0000-0003-1420-6037>
 Michael Cowley  <https://orcid.org/0000-0002-4653-8637>
 Karl Glazebrook  <https://orcid.org/0000-0002-3254-9044>
 Anshu Gupta  <https://orcid.org/0000-0002-8984-3666>
 Glenn G. Kacprzak  <https://orcid.org/0000-0003-1362-9302>
 Lisa Kewley  <https://orcid.org/0000-0001-8152-3943>
 Ivo Labbé  <https://orcid.org/0000-0002-2057-5376>
 Casey Papovich  <https://orcid.org/0000-0001-7503-8482>
 Lee Spitler  <https://orcid.org/0000-0001-5185-9876>
 Caroline M. S. Straatman  <https://orcid.org/0000-0001-5937-4590>
 Adam Tomczak  <https://orcid.org/0000-0003-2008-1752>

References

Alcorn, L. Y., Tran, K.-V., Glazebrook, K., et al. 2018, *ApJ*, 858, 47
 Alcorn, L. Y., Tran, K.-V. H., Kacprzak, G. G., et al. 2016, *ApJL*, 825, L2
 Allen, R. J., Kacprzak, G. G., Glazebrook, K., et al. 2017, *ApJL*, 834, L11

Amorín, R., Fontana, A., Pérez-Montero, E., et al. 2017, *NatAs*, 1, 0052
 Amorín, R., Pérez-Montero, E., Contini, T., et al. 2015, *A&A*, 578, A105
 Amorín, R., Pérez-Montero, E., Vilchev, J. M., & Papaderos, P. 2012, *ApJ*, 749, 185
 Atek, H., Siana, B., Scarlata, C., et al. 2011, *ApJ*, 743, 121
 Bassett, R., Ryan-Weber, E. V., Cooke, J., et al. 2019, *MNRAS*, 483, 5223
 Bian, F., Kewley, L. J., Dopita, M. A., & Juneau, S. 2016, *ApJ*, 822, 62
 Bruzual, G., & Charlot, S. 2003, *MNRAS*, 344, 1000
 Cardamone, C., Schawinski, K., Sarzi, M., et al. 2009, *MNRAS*, 399, 1191
 Ceverino, D., Klessen, R., & Glover, S. 2019, *MNRAS*, 484, 1366
 Cohn, J. H., Leja, J., Tran, K.-V. H., et al. 2018, *ApJ*, 869, 141
 Conroy, C., Gunn, J. E., & White, M. 2009, *ApJ*, 699, 486
 Cowley, M. J., Spitler, L. R., Tran, K.-V. H., et al. 2016, *MNRAS*, 457, 629
 de Barros, S., Vanzella, E., Amorín, R., et al. 2016, *A&A*, 585, A51
 Elbaz, D., Dickinson, M., Hwang, H. S., et al. 2011, *A&A*, 533, A119
 Ferland, G. J., Porter, R. L., van Hoof, P. A. M., et al. 2013, *RMxAA*, 49, 137
 Giacobbe, B., Tran, K.-V. H., Broussard, A., et al. 2017, *ApJL*, 838, L12
 Forrest, B., Tran, K.-V. H., Broussard, A., et al. 2018, *ApJ*, 863, 131
 Forrest, B., Tran, K.-V. H., Tomczak, A. R., et al. 2016, *ApJL*, 818, L26
 Förster Schreiber, N. M., Shapley, A. E., Erb, D. K., et al. 2011, *ApJ*, 731, 65
 Giacconi, R., Zirm, A., Wang, J., et al. 2002, *ApJS*, 139, 369
 Grogin, N. A., Kocevski, D. D., Faber, S. M., et al. 2011, *ApJS*, 197, 35
 Guo, Y., Rafelski, M., Faber, S. M., et al. 2016, *ApJ*, 833, 37
 Ho, L. C., Filippenko, A. V., & Sargent, W. L. W. 1997, *ApJ*, 487, 568
 Holden, B. P., Oesch, P. A., González, V. G., et al. 2016, *ApJ*, 820, 73
 Izotov, Y. I., Guseva, N. G., Fricke, K. J., & Henkel, C. 2016, *MNRAS*, 462, 4427
 Izotov, Y. I., Guseva, N. G., & Thuan, T. X. 2011, *ApJ*, 728, 161
 Izotov, Y. I., Schaerer, D., Worseck, G., et al. 2018, *MNRAS*, 474, 4514
 Jaskot, A. E., & Oey, M. S. 2013, *ApJ*, 766, 91
 Juneau, S., Dickinson, M., Alexander, D. M., & Salim, S. 2011, *ApJ*, 736, 104
 Kacprzak, G. G., van de Voort, F., Glazebrook, K., et al. 2016, *ApJL*, 826, L11
 Kennicutt, R. C. 1998, *ARA&A*, 36, 189
 Koekemoer, A. M., Faber, S. M., Ferguson, H. C., et al. 2011, *ApJS*, 197, 36
 Kriek, M., van Dokkum, P. G., Labbé, I., et al. 2009, *ApJ*, 700, 221
 Kriek, M., van Dokkum, P. G., Whitaker, K. E., et al. 2011, *ApJ*, 743, 168
 Krumholz, M. R., Burkhardt, B., Forbes, J. C., & Crocker, R. M. 2017, arXiv:1706.00106
 Lawrence, A., Warren, S. J., Almaini, O., et al. 2007, *MNRAS*, 379, 1599
 Leja, J., Johnson, B. D., Conroy, C., van Dokkum, P. G., & Byler, N. 2017, *ApJ*, 837, 170
 Lofthouse, E. K., Houghton, R. C. W., & Kaviraj, S. 2017, *MNRAS*, 471, 2311
 Maseda, M. V., van der Wel, A., da Cunha, E., et al. 2013, *ApJL*, 778, L22
 Maseda, M. V., van der Wel, A., Rix, H.-W., et al. 2014, *ApJ*, 791, 17
 Maseda, M. V., van der Wel, A., Rix, H.-W., et al. 2018, *ApJ*, 854, 29
 McLean, I. S., Steidel, C. C., Epps, H. W., et al. 2012, *Proc. SPIE*, 8446, 84460J
 Mitra, S., Ferrara, A., & Choudhury, T. R. 2013, *MNRAS*, 428, L1
 Momcheva, I. G., Brammer, G. B., van Dokkum, P. G., et al. 2016, *ApJS*, 225, 27
 Naidu, R. P., Forrest, B., Oesch, P. A., Tran, K.-V. H., & Holden, B. P. 2018, *MNRAS*, 478, 791
 Nakajima, K., Ellis, R. S., Iwata, I., et al. 2016, *ApJL*, 831, L9
 Nakajima, K., & Ouchi, M. 2014, *MNRAS*, 442, 900
 Nanayakkara, T., Glazebrook, K., Kacprzak, G. G., et al. 2016, *ApJ*, 828, 21
 Nanayakkara, T., Glazebrook, K., Kacprzak, G. G., et al. 2017, *MNRAS*, 468, 3071
 Ouchi, M., Mobasher, B., Shimasaku, K., et al. 2009, *ApJ*, 706, 1136
 Papovich, C., Labbé, I., Quadri, R., et al. 2015, *ApJ*, 803, 26
 Peebles, P. J. E. 1970, *AJ*, 75, 13
 Persson, S. E., Murphy, D. C., Smee, S., et al. 2013, *PASP*, 125, 654
 Reddy, N. A., Shapley, A. E., Sanders, R. L., et al. 2018, *ApJ*, 869, 92
 Roberts-Borsani, G. W., Bouwens, R. J., Oesch, P. A., et al. 2016, *ApJ*, 823, 143
 Robertson, B. E., Ellis, R. S., Furlanetto, S. R., & Dunlop, J. S. 2015, *ApJL*, 802, L19
 Robertson, B. E., Furlanetto, S. R., Schneider, E., et al. 2013, *ApJ*, 768, 71
 Salmon, B., Papovich, C., Finkelstein, S. L., et al. 2015, *ApJ*, 799, 183
 Schmidt, M. 1959, *ApJ*, 129, 243
 Scoville, N., Aussel, H., Brusa, M., et al. 2007, *ApJS*, 172, 1
 Smit, R., Bouwens, R. J., Labbé, I., et al. 2014, *ApJ*, 784, 58
 Spitler, L. R., Straatman, C. M. S., Labbé, I., et al. 2014, *ApJL*, 787, L36
 Straatman, C. M. S., Spitler, L. R., Quadri, R. F., et al. 2016, *ApJ*, 830, 51
 Straughn, A. N., Meurer, G. R., Pirzkal, N., et al. 2008, *AJ*, 135, 1624
 Straughn, A. N., Pirzkal, N., Meurer, G. R., et al. 2009, *AJ*, 138, 1022
 Strom, A. L., Steidel, C. C., Rudie, G. C., et al. 2017, *ApJ*, 836, 164

- Tacconi, L. J., Neri, R., Genzel, R., et al. 2013, [ApJ](#), 768, 74
- Tang, M., Stark, D. P., Chevallard, J., & Charlot, S. 2019, [MNRAS](#), 489, 2572
- Tomczak, A. R., Quadri, R. F., Tran, K.-V. H., et al. 2014, [ApJ](#), 783, 85
- Tomczak, A. R., Quadri, R. F., Tran, K.-V. H., et al. 2016, [ApJ](#), 817, 118
- Tran, K.-V. H., Alcorn, L. Y., Kacprzak, G. G., et al. 2017, [ApJ](#), 834, 101
- Tran, K.-V. H., Nanayakkara, T., Yuan, T., et al. 2015, [ApJ](#), 811, 28
- Trump, J. R., Konidaris, N. P., Barro, G., et al. 2013, [ApJL](#), 763, L6
- Trump, J. R., Sun, M., Zeimann, G. R., et al. 2015, [ApJ](#), 811, 26
- van der Wel, A., Bell, E. F., Häussler, B., et al. 2012, [ApJS](#), 203, 24
- van der Wel, A., Straughn, A. N., Rix, H.-W., et al. 2011, [ApJ](#), 742, 111